ORIGINAL RESEARCH

Improving bifunctional catalytic activity of biochar via in-situ growth of nickel-iron hydroxide as cathodic catalyst for zinc-air batteries

Pengxiang Zhang[1,2†], Kang Sun[3†], Yanyan Liu[1,2,3*] , Benji Zhou[2], Shuqi Li[1], Jingjing Zhou[1], Ao Wang[3], Lixia Xie[1], Baojun Li[2] and Jianchun Jiang[3]

Abstract

Expanding the application scenarios of wood-derived biochar guided by the conversion of traditional energy to new energy shows great promise as a field. As thrilling energy conversion apparatus, zinc-air batteries (ZABs) require cathode catalysts with high oxygen reduction reaction (ORR) and oxygen evolution reaction (OER) activities and stability. Herein, two-dimensional nickel-iron hydroxide nanosheets were creatively assembled in N-doped wood-derived biochar (NiFe-LDH@NC) by an in-situ growth method. The categorized porous organization in wood-derived biochar facilitates the rapid seepage of electrolytes and rapid diffusion of reaction gases. The unique interfacial structure of biochar and NiFe-LDH accelerates electron transfer during oxygen electrocatalysis, and endows NiFe-LDH@NC with first-class catalytic activity and durability for ORR and OER. The ZAB derived from NiFe-LDH@NC showed elevated discharge productivity and cycle endurance, making it promising for viable applications. This work provided a convenient way for the conversion of wood-derived biochar to high-value added electrocatalysts.

Article Highlights

- Heteroatom-doped wood-derived biochar was assisted in situ growth of NiFe-LDH.
- NiFe-LDH@NC exhibited excellent bifunctional activity and stability toward ORR/OER.
- The ZAB achieved a peak power density of 123 mW cm^{-2} and a cycling stability of 270 h.

[†]Pengxiang Zhang and Kang Sun contributed equally to this work.
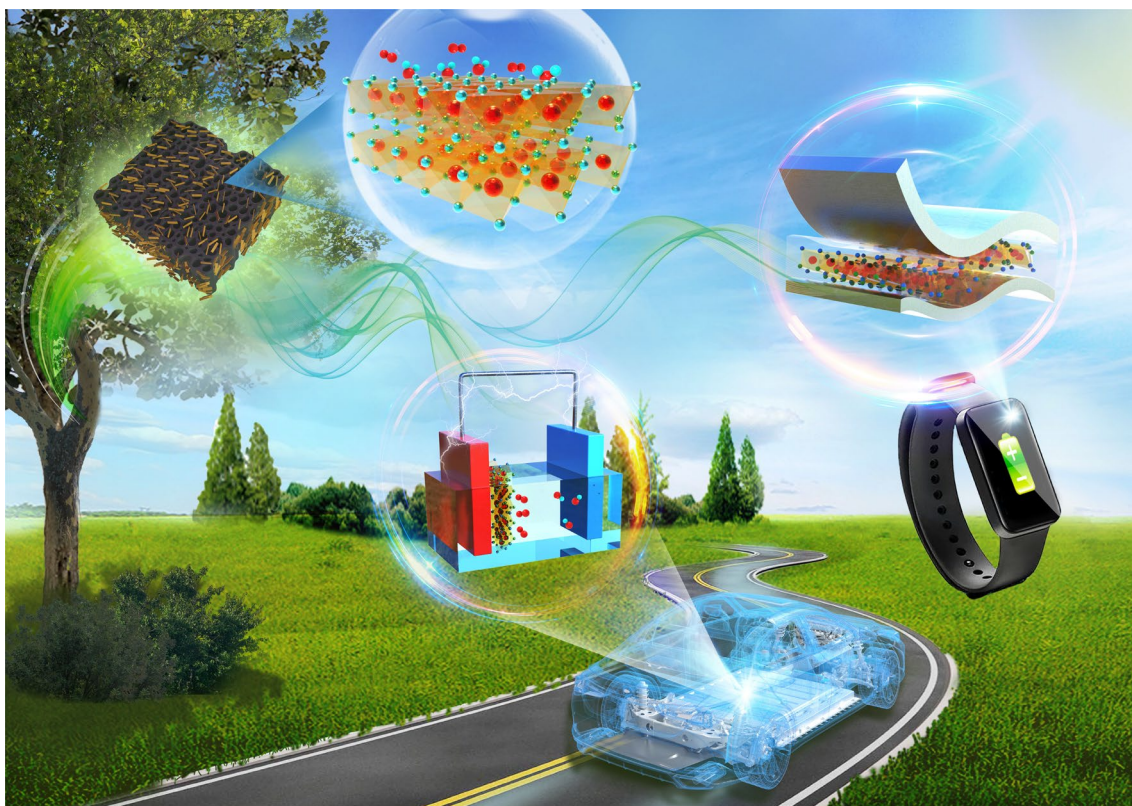
*Correspondence:
Yanyan Liu
lyylhs180208@163.com
Full list of author information is available at the end of the article

Graphical Abstract

1 Introduction

As awareness of ecological protection increases and fossil fuels decline, the shift from traditional energy sources to cleaner and renewable alternatives has become more prominent (Lu et al. 2021; Meftahi et al. 2023b; Yang et al. 2022c). Solving this problem requires the comprehensive development and innovation of electrocatalysis, materials science (Meftahi et al. 2023a), energy storage device technology (Mohassel et al. 2023), and electrochemical sensors (Akbarian et al. 2018; Cheraghi et al. 2022; Sadeghi et al. 2023; Tahernejad-Javazmi et al. 2018; Ziaie and Shabani-Nooshabadi 2023). The most urgent need is to develop efficient energy storage and conversion devices (ESCD) (Meftahi et al. 2022; Shi et al. 2020; Zahedi and Shabani-Nooshabadi 2023). Zinc-air batteries (ZABs) are counted as the most trustworthy next-generation ESCD due to their high energy density, safety and non-pollution (Lee et al. 2022). The energy efficiency during the charge-discharge operation of ZABs is determined by two oxygen-related reactions at the cathode (Liu et al. 2022b; Lu et al. 2022). Regrettably, the kinetics of both oxygen reduction reaction (ORR) and oxygen evolution reaction

(OER) are hostile in the absence of catalysts (Tian et al. 2019). The lack of effective catalysts severely obscures the large-scale application prospects of ZABs (Yan et al. 2020b). Designing and constructing efficient catalysts for ORR & OER using sustainable resources is decisive to enhance the energy conversion efficiency of ZABs (Mehmood et al. 2022).

The synthesis and production processes of traditional carbon materials mainly relies on fossil energy (Jiang et al. 2021; Yang et al. 2022b). The high energy consumption and low sustainability of traditional carbon-based composite catalysts make them unsuitable for large-scale production and application (Liu et al. 2019; Zhu and Mu 2020). Wood-derived biochar comes from green and renewable raw materials and can inherit the structural advantages of wood's hierarchical and hierarchical pores in subsequent processing (Sakhiya et al. 2020). The three-dimensional interconnected channels facilitate the anchoring of metal active sites and mass transport in electrocatalytic reactions (Gabhi et al. 2020). Rational heteroatom doping of wood-derived biochar materials yields unique biochar-based catalysts with self-supporting

structures (Hui et al. 2022; Yan et al. 2022a). In ESCD, wood-derived biochar can also be directly used as an air electrode (Chen et al. 2017; Song et al. 2018). However, air electrodes composed only of heteroatom-doped biochar materials have insufficient active sites and cannot simultaneously have efficient ORR and OER catalytic dual functions to satisfy ZABs (Peng et al. 2019). Hence, an straightforward and efficient approach for fabricating effective electrocatalysts based on wood-derived biochar composites should be determined to fulfill the requirements of the emerging generation of ESCDs.

The unique structural features and catalytic properties of layered double hydroxides (LDHs) have made them a focus of attention in the field of electrocatalysts (Pei et al. 2019). LDHs, consisting of metal cations coordinated with hydroxide as the main layer and various anions in the interlayer structure, offer a promising platform for designing and modulating versatile catalytic active sites (Niu et al. 2022; Wang et al. 2020). The two-dimensional sheet-like morphology of LDHs allows for large amounts of active sites to be exposed, resulting in excellent catalytic activity (Lu et al. 2020). This unique composition including the main layer and the interlayer structure endows LDHs with adjustable composition of each layer (Wang et al. 2022). These characteristics make LDHs attract a lot of research interest in the field of electrocatalysis (Niu et al. 2022). For example, through the electronic modulation between divalent nickel ions and ferric ions, suitable adsorption and desorption manners for the reaction intermediates during OER process can be obtained on NiFe-LDHs (He et al. 2022). The catalytic activity of NiFe-LDHs is not ideal toward ORR, mainly restricted by the low electrical conductivity (EC), lack of active sites and insufficient surface area. To meet the requirement of bifunctional air electrodes, NiFe-LDHs are combined with carbon supports to obtain excellent overall ORR and OER activities (Lv et al. 2020). Carbon supports (carbon nanotubes, graphene, carbon paper, etc.) possessing large surface areas and high EC usually are used to improve catalytic performance (Yan et al.

2020b). Doping different heteroatoms subsequently optimized carbon supports to boost the bifunctional activity of NiFe-LDHs (He et al. 2022). However, the micro-scale morphology of LDHs creates barriers to the facile and effective combination with nanoporous carbon materials (Zhan et al. 2017). A feasible and well-organized strategy can be developed to construct bifunctional catalysts with wood-derived biochar supports and NiFe-LDH nanosheets, featuring tight anchoring and bonding, to enhance the catalytic performance.

In this work, two-dimensional NiFe-LDHs were constructed in a three-dimensional hierarchical porous nitrogen-doped carbon support. The strategy of support-assisted in situ hydrothermal growth resulted in a composite catalyst NiFe-LDH@NC (Fig. 1). The physicochemical properties and oxygen electrocatalytic performances were evaluated through a series of analytical and characterization techniques. The NiFe-LDH@NC expressed excellent ORR and OER bifunctional catalytic activity and robust stability. The ZABs assembled with NiFe-LDH@NC catalyst exhibited extremely high power density and superior cycling stability. This research provided a proof-of-concept for the implementation of the interaction between wood-derived biochar supports and transition metal active matters.

2 Results and discussion
2.1 Morphological and structural characterization of catalysts
To reveal the structural heredity and possible change, the microscopic morphology of NC, NiFe-LDH, and NiFe-LDH@NC were observed by scanning electron microscopy (SEM) (Fig. 2a–f). After nitrogen doping treatment, the three-dimensional porous microchannels and straight channels along the growth side of the tree trunk were preserved in NC (Fig. 2a). The uniformly arranged polygonal channels mostly had a diameter of 5–20 µm. After nitrogen doping treatment, abundant holes were still observed from the side view of NC (Fig. 2d). The existence of these pores connects the internal structure
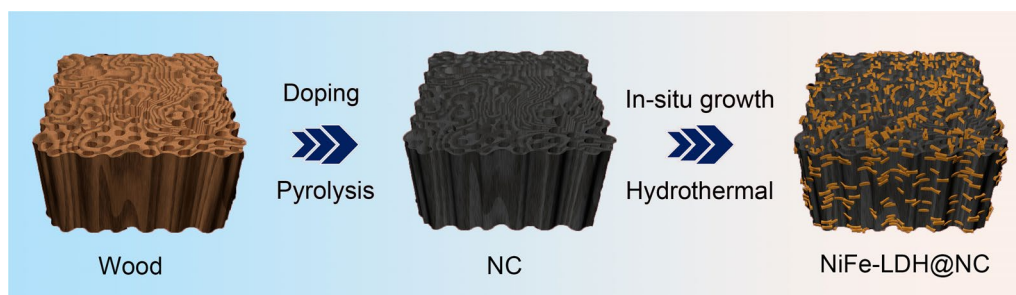

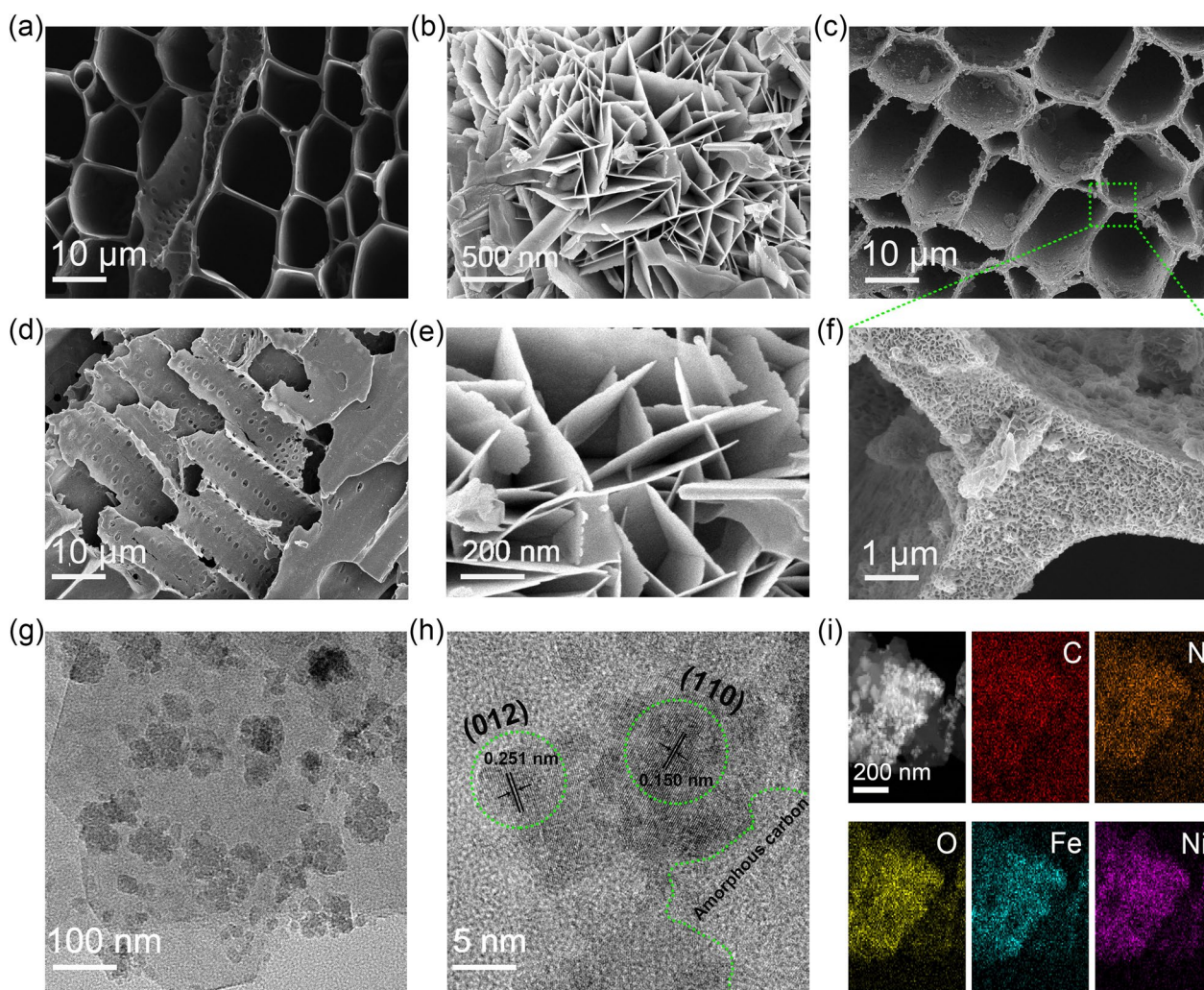**Fig. 1** Preparation process of NiFe-LDH@NC composite catalyst

Fig. 2 SEM images of **a** NC, **b**, **e** NiFe-LDH, **c**, **f** NiFe-LDH@NC; **d** SEM images showing the cross-sectional view of NC; **g** TEM **h** HR-TEM images and **i** Element mapping images of NiFe-LDH@NC

of NC. The mass transfer efficiency inside porous carbon contributes to the hydrothermal growth of NiFe-LDH (Zhou et al. 2022). The NiFe-LDH has a smooth two-dimensional nanosheet structure (Fig. 2b). The enlarged SEM image showed the thinner lamellae of the generated NiFe-LDH (Fig. 2e). The growth of NiFe-LDH on the surface of NC could be observed on a larger scale as shown in Fig. 2c and f. The 3D structure of NC allows for the uniform accommodation of NiFe-LDH nanosheets. Atomic force microscopy (AFM) was used to better understand the surface morphology of NiFe-LDH@ NCs. In NiFe-LDH@NC, NiFe-LDH was uniformly dispersed on the monolithic NC surface with a height of 1 μm NiFe-LDH nanosheet (Additional file 1: Fig. S1a, b). 3D AFM topography (Additional file 1: Fig. S1c) visualized appears the above structure. To further characterize the fine structure of NiFe-LDH@NC, transmission

electron microscopy (TEM) was used. Plate-like NiFe-LDH metal particles supported on amorphous NCs can be seen in Fig. 2g. The (012) plane of 0.251 nm and the (110) plane of 0.150 nm lattice spacing attributed to NiFe-LDH were surrounded by amorphous NCs. The high-resolution TEM (HR-TEM) confirmed the successful preparation of NiFe-LDH@NC composites (Fig. 2h) (Yang et al. 2019; Zhan et al. 2017). The element distribution diagram shows elements (C, N, O, Fe, Ni) were uniformly dispersed in NiFe-LDH@NC (Fig. 2i). The element distribution diagram also explains the uniform dispersion of C, N, O, Fe, Ni in NiFe-LDH@NC. The nanosheet-like structure of NiFe-LDH and the hierarchically porous structure of NC were well preserved in NiFe-LDH@NC. The successful synthesis of the anticipated catalyst structure was endorsed by the morphological and structural analysis, with the nanosheet-like structure of NiFe-LDH

and the hierarchically porous structure of NC both preserved in NiFe-LDH@NC.

2.2 Phase and structural characterization of catalysts

The phases of NiFe-LDH@NC, NC and CW as comparative samples were investigated by X-ray diffraction (XRD) (Additional file 1: Fig. S2a). Among the diffraction peaks of the XRD patterns of NC and CW, there are diffraction peaks of the C (002) crystal plane and the C (101) crystal plane of carbon. The broad diffraction peaks reflect the amorphous structure of carbon materials from the forest trees (Yuan et al. 2020). The right shifting C (002) peak position of NC can be attributed to the enhanced interlayer interaction of carbon. The decrease in the interlayer spacing of carbon should be due to the doping of nitrogen element (Wu et al. 2019). In the XRD pattern of NiFe-LDH@NC, the diffraction peaks match with (003), (006), (012), (015), (018), (110), (113) crystal planes in the NiFe-LDH standard card (PDF #40-0215). The C (002) diffraction peak corresponding to NC can also be found at 23.8° (Zhan et al. 2017). The results obtained from XRD, corresponding to the conclusions from HRTEM, prove the successful synthesis of NiFe-LDH@NCs containing both NC supports and NiFe-LDH.

The Raman spectroscopy analysis reveals that the structure of carbon defects in NC, CW, and NiFe-LDH@NC. Specifically, the D peak observed at 1340 cm^{-1} was described to the amorphous defective structure of sp^3 hybrid carbon, whilst the G peak at 1590 cm^{-1} was described to the stretching vibration of sp^2 hybridized carbons (Tang et al. 2018). The ratio of the D peak to the G peak (I_D/I_G) is a foremost parameter that reflects the defects of carbon materials (Chen et al. 2020). The I_D/I_G of NC, NiFe-LDH@NC and CW were 1.07, 1.04 and 1.01, respectively (Additional file 1: Fig. S2b). These values suggest that all three materials have many edge carbon defect structures. The I_D/I_G value of NC was found to be higher than that of CW, representing that nitrogen doping treatment can upgrade the disposition of carbon defects in the material. The area ratios corresponding to the D band and the G band, that is, the frequency integrated intensity ratio (A_D/A_G), were 3.35, 3.15, and 2.61, respectively. The highly defective carbon structure in NiFe-LDH@NC, as indicated by its I_D/I_G and A_D/A_G value similar to that of NC, is expected to contribute to the improved catalytic activity of the compound (Hu et al. 2021; Zhao et al. 2020).

X-ray photoelectron spectroscopy (XPS) was used to investigate surface element composition, valence, and bonding. The XPS survey spectra of NiFe-LDH@NC displayed peaks with contents of 65.17% atom, 1.92% atom, 22.42% atom, 2.63% atom, and 7.84% atom for C 1s, N 1s, O 1s, Fe 2p, and Ni 2p, respectively (Additional

file 1: Fig. S2c). This confirms that NIFe-LDH is a Ni$_3$Fe-LDH structure with a Ni:Fe ratio of 3:1. The C 1s peak of NiFe-LDH@NC separated into C=C (284.8 eV), C–C (285.5 eV), C–O (287.8 eV), and O–C=O (291.2 eV) (Fig. 3a). The N 1s spectra of NiFe-LDH@NC closely match four peaks at 398.5 eV, 399.8 eV, 401.2 eV, and 406.3 eV, corresponding to pyridine, pyrrole, graphite, and oxide-type N doping, respectively (Fig. 3b) (Yan et al. 2020a). The Ni 2p spectra of NiFe-LDH@NC and NiFe-LDH are shown in Fig. 3c. The peaks of NiFe-LDH@NC at 857.9 eV and 875.5 eV, corresponding to Ni 2p$_{1/2}$ and Ni 2p$_{3/2}$, exhibit a shift of 1.5 eV towards higher energy compared to NiFe-LDH. On the other hand, in the Fe 2p region (Fig. 3b), the peaks for Fe^{3+} on NiFe-LDH@NC are red-shifted compared to 712.2/726.2 eV on NiFe-LDH (Yan et al. 2022b). The electron transfer from NiFe-LDH to NC leads to the shifting of Fe 2p and Ni 2p peaks. The high electronegativity of nitrogen-doped carbon and the electron-withdrawing phenomenon cause electron transfer (Lv et al. 2020; Ye et al. 2021). This metal-support interaction facilitates charge transfer at the interface of the heterostructure. The charge transfer enriches the electron density of NC (Chen et al. 2021).

2.3 Oxygen electrocatalytic performance

First, the CV curves of NiFe-LDH@NC, 20% Pt/C, NC, and NiFe-LDH in nitrogen or oxygen saturated electrolytes were measured (Additional file 1: Fig. S3). In the oxygen-saturated electrolyte, all four materials provided obvious reduction potentials. In the nitrogen-saturated electrolyte, no reduction potentials indicated unique catalytic activities to ORR for the above materials. The reduction potential of NiFe-LDH@NC was between 0.80 and 0.90 V. That of NC was between 0.65 and 0.75 V, and that of NiFe-LDH was between 0.50 and 0.60 V. The reduction potential of 20% Pt/C around 0.83 V was most close to that of NiFe-LDH@NC. This similar potential indicates a similar ORR catalytic ability for NiFe-LDH@NC to 20% Pt/C.

Linear sweep voltammetry (LSV) was used to investigate the catalytic capabilities of NiFe-LDH@NC, NC, and NiFe-LDH with commercial 20% Pt/C as the standard ORR catalyst and RuO$_2$ as the common OER catalyst. The produced materials were used to compare the catalytic performance. NiFe-LDH@NC had an onset potential in ORR (0.90 V), which was similar to Pt/C (0.94 V) but greater than NC (0.82 V) and NiFe-LDH (0.76 V) (Fig. 4a). The ORR half-wave potential ($E_{1/2}$) on NiFe-LDH@NC was 0.83 V, which was comparable to 0.84 V for Pt/C and higher than 0.67 V for NiFe-LDH and 0.78 V for NC. NiFe-LDH@NC had a higher limiting current density of up to 5.96 mA cm^{-2} than Pt/C (5.92 mA cm^{-2}), and NC (4.88 mA cm^{-2}). NiFe-LDH had a
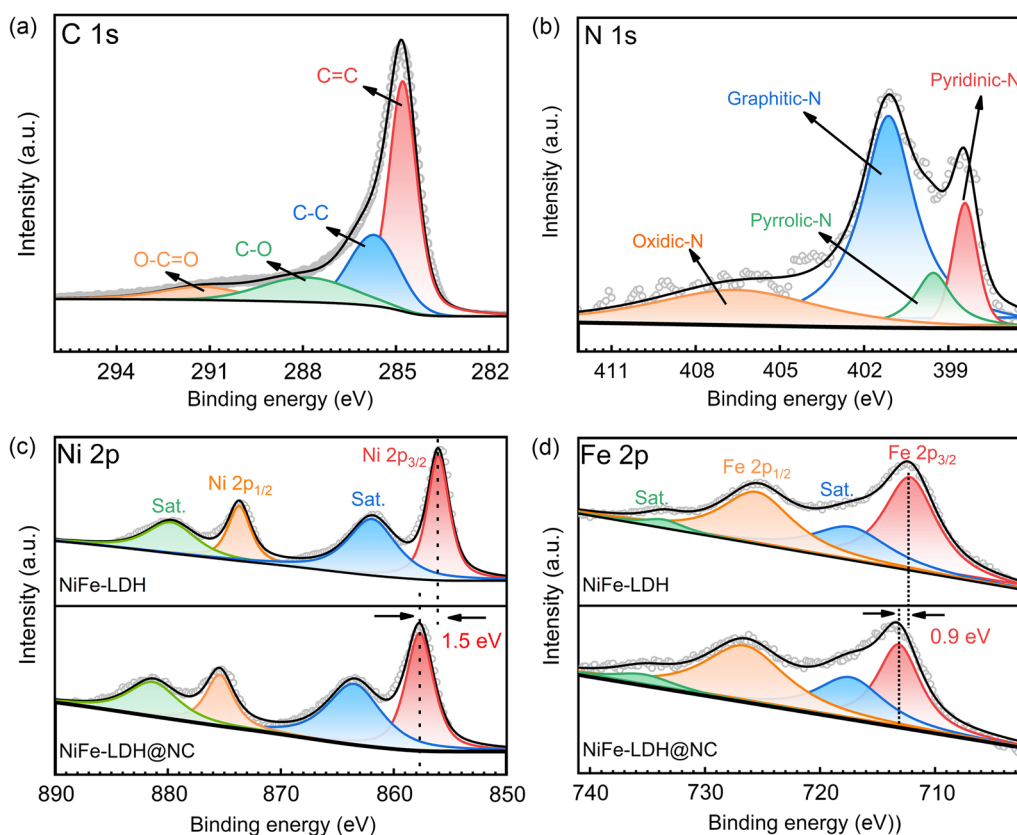
Fig. 3 **a** C 1s **b** N 1s spectrum of NiFe-LDH@NC; **c** Ni 2p and **d** Fe 2p spectra of NiFe-LDH@NC and NiFe-LDH
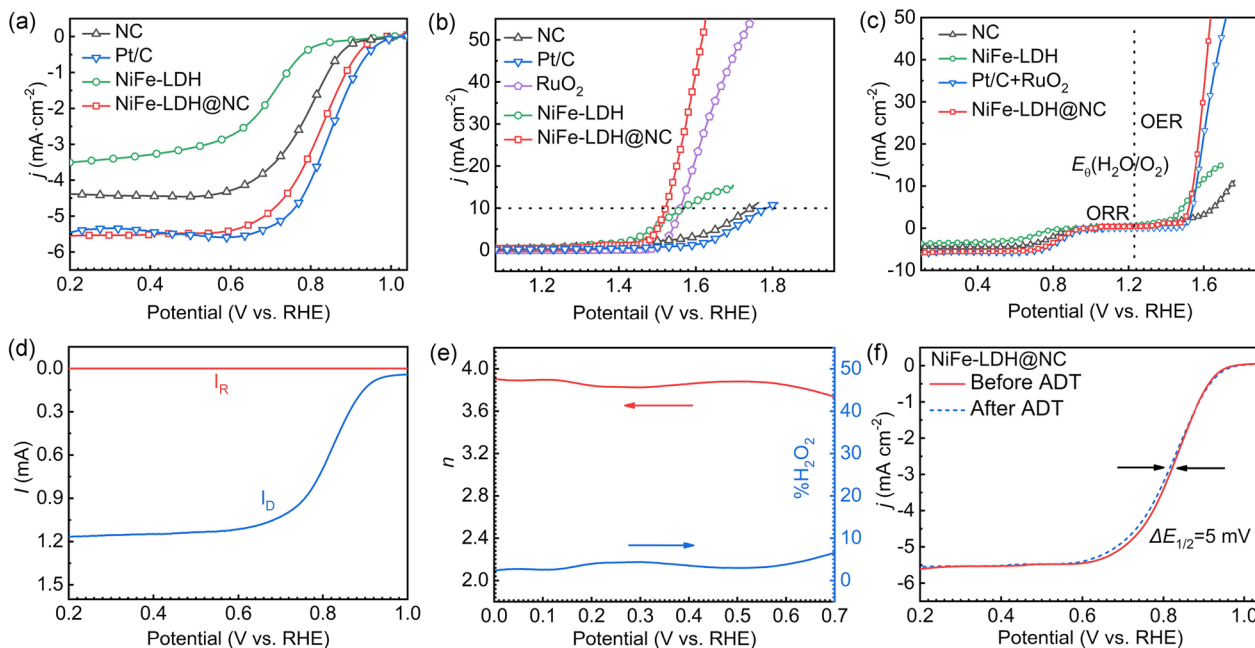

Fig. 4 LSV curves of **a** ORR and **b** OER; **c** LSV curves and ΔE of NiFe-LDH@NC, NiFe-LDH, 20% Pt/C + RuO$_2$ and NC; **d** RRDE curves of NiFe-LDH@NC; **e** The n and H$_2$O$_2$ percentage of NiFe-LDH@NC; **f** LSV comparison before and after ADT test

smaller limiting current density (3.65 mA cm^{-2}) because of its weak conductivity. The larger $E_{1/2}$ and increased maximum current density show that NiFe-LDH@NC has outstanding ORR catalytic activity. In addition, the Tafel curves obtained from the LSV measurements of the ORR demonstrated that the Tafel slopes for NiFe-LDH@NC, NC, NiFe-LDH, and 20% Pt/C catalysts were 121, 124, 132, and 126 mV dec^{-1}, respectively (Additional file 1: Fig. S4). The lower Tafel slope of NiFe-LDH@NC indicates its superior catalytic activity and efficiency in ORR compared to the other catalysts. The obtained samples were also tested by electrical impedance spectroscopy (EIS) (Additional file 1: Fig. S5). The minimum charge transfer resistance indicates the fastest charge transfer kinetics for ORR on NiFe-LDH@NC.

Figure 4b shows the LSV curves with RuO$_2$, NiFe-LDH@NC, 20% Pt/C, NC, and NiFe-LDH for OER. The overpotentials of NC, NiFe-LDH, RuO$_2$, and 20% Pt/C were 520 mV, 420 mV, 340 mV, and 550 mV (at 10 mA cm^{-2}), respectively. The overvoltage of NiFe-LDH@NC was impressively low at 310 mV. Comparing the limiting current of the LSV curves of NiFe-LDH and NiFe-LDH@NC in OER, the designed NiFe-LDH@NC composite showed a higher limiting current than that of NiFe-LDH. Due to the compounding of LDH with biochar, the EC of the compound was improved. NiFe-LDH@NC can speed up the reaction at higher current density. The bifunctional activity of catalysts can be estimated from the voltage difference between ORR and OER ($\Delta E = E_{OER}-E_{ORR}$) (Wu et al. 2020). The ΔE of NiFe-LDH@NC of 0.72 V was comparable to that of Pt/C+RuO$_2$ (0.72 V), and lower than 1.09 V for NiFe-LDH and 0.97 V for NC (Fig. 4c). NiFe-LDH@NC provided a similar ΔE to that of commercial noble metal catalysts. The ΔE value of NiFe-LDH@NC reflects the achievement of bifunctional catalytic activity comparable to noble metal catalysts at low cost.

During the ORR of NiFe-LDH@NC, the electron transfer number (n) and the hydrogen peroxide yield (H$_2$O$_2$%) were estimated using a rotating annular disc electrode (RRDE) (Fig. 4d). In the voltage range of 0–0.7 V, the n of NiFe-LDH@NC ranged from 3.83 to 3.92, and the H$_2$O$_2$ percentage was constantly below 7%. Based on the recorded LSV curves of the ORR conducted at various rotational speeds (400–2025 rpm), the average n value calculated using the Koutecký-Levich (KL) equation was 4.1 (Additional file 1: Fig. S6). The n value close to 4 indicates that the ORR on NiFe-LDH@NC proceeds according to the 4e$^-$ reaction with excellent catalytic selectivity for the 4e$^-$ path (Wang et al. 2021; Xie et al. 2022). The durability of the catalyst was estimated by accelerated durability test (ADT). The $E_{1/2}$ of NiFe-LDH@NC had only a slight negative displacement of 5

mV after ADT with unchanged limiting current (Fig. 4f). The $E_{1/2}$ of commercial 20% Pt/C after ADT dropped by 35 mV (Additional file 1: Fig. S7). The negligible decay of $E_{1/2}$ before and after ADT proves the superb catalytic durability of NiFe-LDH@NC.

The stability of the catalysts was characterized by chronoamperometry (CP) (Yang et al. 2022a). For ORR, the current density retention was kept at 89% for NiFe-LDH@NC and 51% for 20% Pt/C after 12 h. The NiFe-LDH@NC expressed no obvious current attenuation (8 mV) after CP test, while 20% Pt/C attenuated a lot (92 mV) (Additional file 1: Fig. S8a–c). The OER CP curves of NiFe-LDH@NC and RuO$_2$ were tested at the voltage corresponding to 10 mA cm^{-2}. NiFe-LDH@NC showed a current density retention of 94% after testing, while RuO$_2$ had a retention of only 67% (Additional file 1: Fig. S8d). The overpotential of NiFe-LDH@NC at 10 mA cm^{-2} increased by 15 mV and that of RuO$_2$ by 37 mV (Additional file 1: Fig. S8e, f). The CP test confirmed the excellent bifunctional long-term catalytic durability of NiFe-LDH@NC.

The ability to resist organic poisoning is also important in evaluating the catalytic stability of catalysts. The excellent anti-toxicity enables the catalysts to reliably exert catalytic vocation under complex and changeable reaction conditions (Li et al. 2022; Zhou et al. 2021). The methanol poisoning tests of NiFe-LDH@NC and 20% Pt/C were conducted for comparison. After methanol poisoning test, the current density decay rate of NiFe-LDH@NC was 11.5%, and that of Pt/C was 53.9% (Additional file 1: Fig. S8g). By comparing the LSV polarization curves of the two catalytic materials before and after the test, the $E_{1/2}$ of NiFe-LDH@NC was attenuated by 20 mV (Additional file 1: Fig. S8h). The E$_{1/2}$ of 20% Pt/C was attenuated by 44 mV (Additional file 1: Fig. S8i). From the organic poisoning test results, NiFe-LDH@NC showed excellent anti-poisoning ability to effectively resist the shuttle effect of organic by-products during the reaction process (Feng et al. 2022). After undergoing electrochemical testing, the NiFe-LDH@NC catalyst was subjected to XRD and XPS analyses. There were no significant changes observed in the XRD and XPS spectra when compared to the initial NiFe-LDH@NC (Additional file 1: Fig. S9). The results reveals that the crystal structure and surface electronic state of the catalyst remained unchanged after the electrochemical testing, highlighting the excellent stability of NiFe-LDH@NC.

2.4 Applications of NiFe-LDH@NC in zinc-air batteries

A ZAB was assembled using NiFe-LDH@NC as the air electrode catalyst, while a ZAB constructed with Pt/C and RuO$_2$ (1:1 mass ratio) as the air electrode catalyst was used as a benchmark. The open circuit voltage (OCV)

performance of the ZAB-based NiFe-LDH@NC (1.44 V) can be comparable to that of the ZAB with Pt/C + RuO$_2$ (1.45 V) (Fig. 5a). The discharge/charge polarization curves disclosed that the NiFe-LDH@NC-based ZAB exhibited a smaller voltage gap during discharge/charge. When the current density reached 10 mA cm^{-2}, the voltage gap of NiFe-LDH@NC was 0.52 V (0.69 V for Pt/C + RuO$_2$) (Additional file 1: Fig. S10). The discharge curve and the corresponding power density curve of the ZABs are shown in Fig. 5b. The peak power density of the NiFe-LDH@NC mounted ZAB was 123 mW cm^{-2} at 1.23 V, surpassing that of the Pt/C + RuO$_2$ mounted ZAB (64 mW cm^{-2} at 0.62 V). Compared to Pt/C + RuO$_2$, the ZAB was greatly improved with NiFe-LDH@NC. Galvanostatic charge-discharge tests were performed to investigate the cycling stability of batteries made from different catalytic materials. At 10 mA cm^{-2}, the stable cycle time of the ZAB based on NiFe-LDH@NC

over 270 h (810 cycles) was significantly higher than that found on Pt/C + RuO$_2$ (85 h) (Fig. 5c). The gap between the charge voltage and discharge voltage of NiFe-LDH@NC was more stable during the test. The charge-discharge test results confirmed the long-term operational stability of the ZAB assembled with NiFe-LDH@NC (Li et al. 2022). Furthermore, NiFe-LDH@NC-based aqueous ZABs were able to successfully drive light bulbs and LED lamp beads (Additional file 1: Fig. S11). The performance of ZAB based on NiFe-LDH@NC was at the forefront among similar biochar-related catalysts (Additional file 1: Table S1). One of the major advantages of NiFe-LDH@NC, as a wood-derived biochar-based composite, was that it can be directly used as a monolithic catalyst. The quasi-solid ZABs were assembled using the monolithic NiFe-LDH@NC as the air electrode, PVA gel as the electrolyte, and zinc foil as the anode (Liu et al. 2021). The results are shown in Fig. 5d, and the OCV of
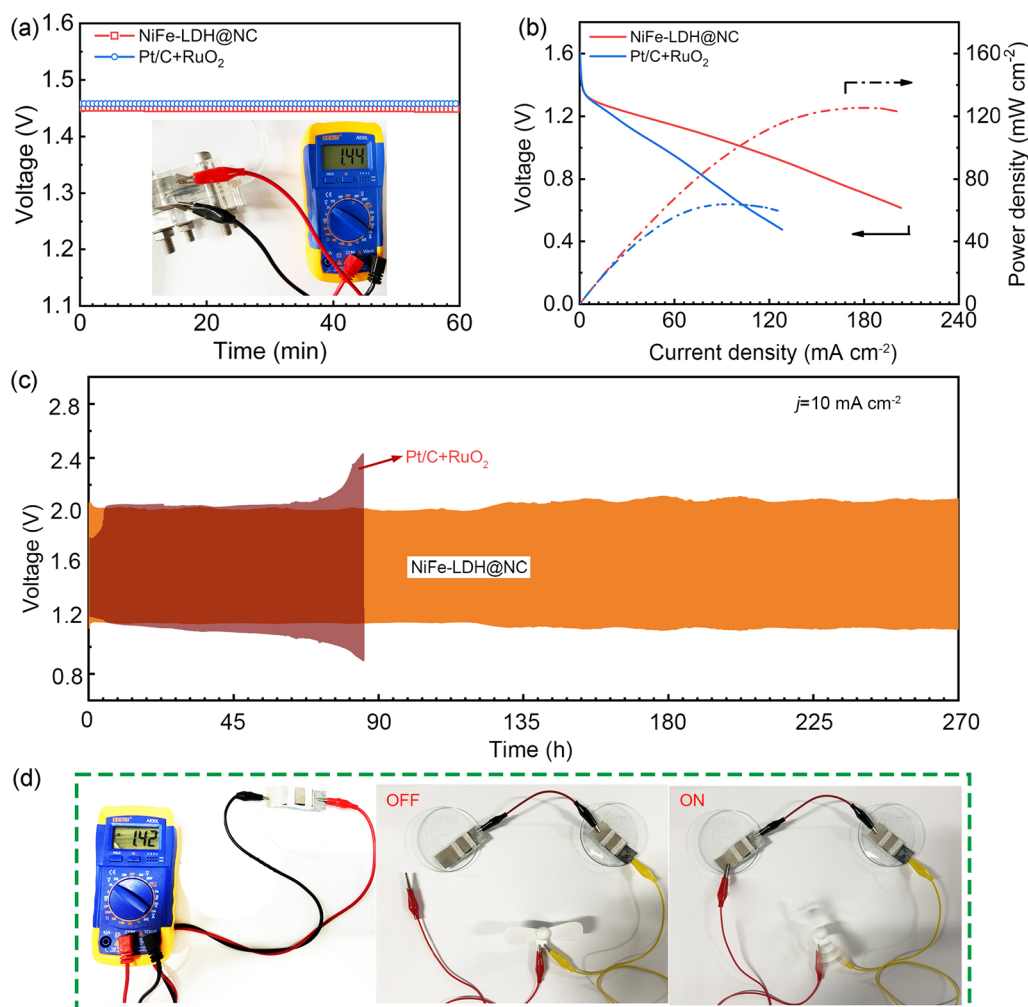

Fig. 5 a OCV curves **b** discharge curves and **c** cycling test of aqueous ZABs constitutional by NiFe-LDH@NC and Pt/C + RuO$_2$; **d** images of OCV and drive fan for quasi-solid-state ZAB with NiFe-LDH@NC

the assembled quasi-solid ZAB reached up to 1.42 V. Two NiFe-LDH@NC-based quasi-solid ZABs in series can be directly used as a power source to drive the fan to rotate. The above results demonstrate the great potential of NiFe-LDH@NC as a catalyst for ZABs.

2.5 Study of the structure–activity relationship

A structure–activity relationship for the ORR and OER catalyzed by NiFe-LDH@NC was proposed based on the above analysis (Fig. 6). (I) The doping of N heteroatoms improves the conductivity of the biochar and generates abundant defects in the carbon layer (Ye et al. 2020). The generation of defects favors the bulk anchoring of metal sites. NC as a supporter provides excellent conductivity and dispersion for metal active sites, which is beneficial to preventing metal aggregation and exposing more accessible active sites (Niu et al. 2021). (II) The rich pore structure of natural wood is preserved during the treatment. The hierarchical porous structure facilitates the rapid transport and diffusion of active species such as O_2 and oxygen-containing intermediates in the oxygen electrocatalytic process (Chen et al. 2019). (III) During the ORR process, the C atoms in NiFe-LDH@NC serve as active sites for O_2 adsorption and activation in ORR (Liang et al. 2014). The adjacent NiFe(OH) sites fine-tune the electron density arrangement around the C sites accelerate the splitting of water molecules to generate protons required for ORR (Zhang et al. 2022), and improve the ORR catalytic activity. (IV) During OER, the high voltage required for OER causes the NiFe-LDH on the surface of NiFe-LDH@NC to be oxidized and converted into metal-oxyhydroxide in situ (Bai et al. 2021). The metal-oxyhydroxide acts as the real active center of OER to catalyze the OER reaction (Ni or Fe sites) (Liu

et al. 2022a). Due to its unique structure, NiFe-LDH@NC will generate abundant metal-oxyhydroxides for OER. In addition, it cannot be ignored that some lattice oxygen will be generated during the oxidation of NiFe-LDH to NiFeOOH. The lattice oxygen in NiFe-LDH@NC can also act as active sites for OER (Liu et al. 2023). The lattice oxygen mechanism (LOM) can break the linear constraint of the intermediate transition state of traditional metal redox chemistry of adsorption evolution mechanism (AEM), and reduce the overall overpotential of OER (Wang et al. 2023). In summary, this dynamic switching and multi-catalytic site synergy of NiFe-LDH@NC achieves high-efficiency bifunctional catalytic activity.

3 Conclusions

In conclusion, a heterostructure NiFe-LDH@NC composed of 3D biochar supports and 2D nanosheets was constructed by in situ growth to advance the catalytic activity of oxygen conversion. The hierarchical porous structure in the wood-derived biochar facilitates fast electrolyte penetration. The wood-derived biochar and NiFe-LDH combination enhanced the composite's overall electrocatalytic capability and facilitated the electron transfer during catalysis. The NiFe-LDH@NC exhibited excellent ORR and OER catalytic activity and steady stability. The ZAB assembled with NiFe-LDH@NC showed decent power density and cycling stability. The quasi-solid-state ZAB assembled directly as a monolithic electrode by NiFe-LDH@NC still demonstrated its practical value. This research provided inspiring ideas for the economic development, deployment and transformation of wood-derived biochar to high value-added electrocatalyst.
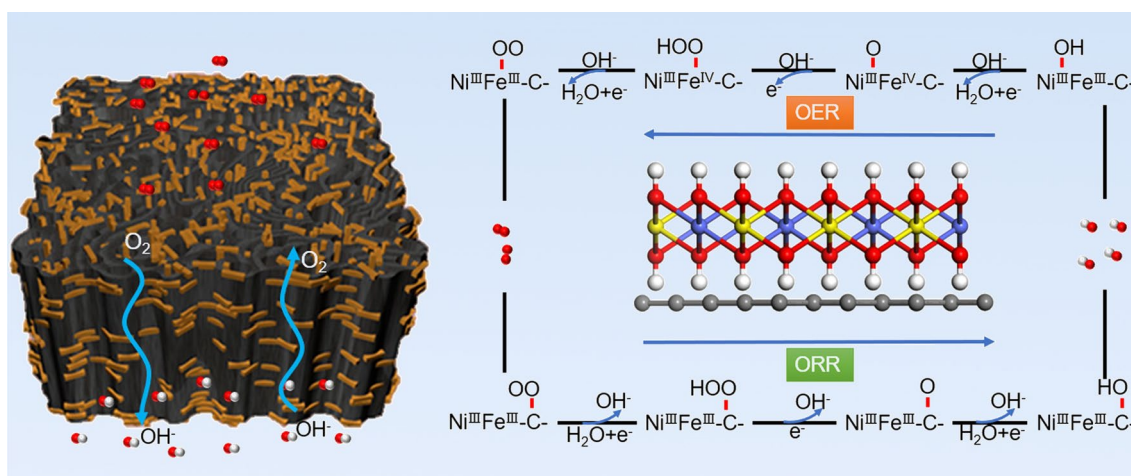

Fig. 6 Structure–activity relationship of ORR and OER at NiFe-LDH@NC

Supplementary Information

The online version contains supplementary material available at https://doi.org/10.1007/s42773-023-00259-1.

Additional file 1. Material synthesis, characterization methods and some raw data. **Fig. S1.** AFM characterization of NiFe-LDH@NC. **Fig. S2.** XRD, Raman, XPS spectrum of materials. **Fig. S3.** CV curves of NiFe-LDH@NC, 20% Pt/C, NC and NiFe-LDH. **Fig. S4.** The Tafel slope corresponding to the LSV curve of ORR. **Fig. S5.** Nyquist plots of NiFe-LDH@NC, NC, NiFe-LDH. **Fig. S6.** LSV curves of ORR at different rotational speeds (400~2025 rpm) and corresponding K-L diagrams at different potentials. **Fig. S7.** LSV curves of 20% Pt/C before and after ADT. **Fig. S8.** Electrochemical stability test of NiFe-LDH@NC and Pt/C. **Fig. S9.** XRD and XPS spectra of NiFe-LDH@NC after electrochemical test. **Fig. S10.** Discharge and charge polarization curves of NiFe-LDH@NC. **Fig. S11.** Demonstration of actual usage scenarios of ZAB based on NiFe-LDH@NC. **Table S1.** Important parameters comparison of biochar-related catalysts for zinc-air batteries.

Author contributions
PZ: Investigation, formal analysis, visualization, writing—review and editing. KS: Investigation, writing—review and editing. YL: Design, formal analysis, investigation, supervision. BZ: Methodology, investigation, visualization, formal analysis. SL: Investigation, writing—review and editing. JZ: Investigation, writing—review and editing. AW: Investigation, formal analysis, conceptualization. LX: Formal analysis, supervision, investigation visualization. BL: Formal analysis, supervision, conceptualization. JJ: Design, formal analysis, supervision, visualization.

Data availability
Data of this work will be made available for reasonable reason.

Declarations

Competing interests
The authors have no relevant financial or non-financial interests to disclose.

Author details
[1]College of Science, Henan Agricultural University, Zhengzhou 450002, China. [2]College of Chemistry, Zhengzhou University, Zhengzhou 450001, China. [3]Institute of Chemical Industry of Forest Products, Chinese Academy of Forestry (CAF), Nanjing 210042, China.

References

Akbarian Y, Shabani-Nooshabadi M, Karimi-Maleh H (2018) Fabrication of a new electrocatalytic sensor for determination of diclofenac, morphine and mefenamic acid using synergic effect of NiO-SWCNT and 2, 4-dimethyl-N/-[1- (2, 3-dihydroxy phenyl) methylidene] aniline. Sens Actuators B 273:228–233. https://doi.org/10.1016/j.snb.2018.06.049

Bai L, Lee S, Hu X (2021) Spectroscopic and electrokinetic evidence for a bifunctional mechanism of the oxygen evolution reaction*. Angew Chem Int Ed Engl 60(6):3095–3103. https://doi.org/10.1002/anie.202011388

Chen C, Zhang Y, Li Y, Dai J, Song J, Yao Y, Gong Y, Kierzewski I, Xie J, Hu L (2017) All-wood, low tortuosity, aqueous, biodegradable supercapacitors with ultra-high capacitance. Energy Environ Sci 10(2):538–545. https://doi.org/10.1039/c6ee03716j

Chen C, Xu S, Kuang Y, Gan W, Song J, Chen G, Pastel G, Liu B, Li Y, Huang H, Hu L (2019) Nature-inspired Tri-pathway design enabling high-performance flexible Li–O₂ batteries. Adv Energy Mater 9(9):1802964. https://doi.org/10.1002/aenm.201802964

Chen G, Liu P, Liao Z, Sun F, He Y, Zhong H, Zhang T, Zschech E, Chen M, Wu G, Zhang J, Feng X (2020) Zinc-mediated template synthesis of Fe-N-C electrocatalysts with densely accessible Fe-N$_x$ active Sites for efficient oxygen reduction. Adv Mater 32(8):1907399. https://doi.org/10.1002/adma.201907399

Chen Q, Gong N, Zhu T, Yang C, Peng W, Li Y, Zhang F, Fan X (2021) Surface phase engineering modulated iron-nickel nitrides/alloy nanospheres with tailored d-band center for efficient oxygen evolution reaction. Small 18(4):2105696. https://doi.org/10.1002/smll.202105696

Cheraghi S, Taher MA, Karimi-Maleh H, Karimi F, Shabani-Nooshabadi M, Alizadeh M, Al-Othman A, Erk N, Yegya Raman PK, Karaman C (2022) Novel enzymatic graphene oxide based biosensor for the detection of glutathione in biological body fluids. Chemosphere 287(2):132187. https://doi.org/10.1016/j.chemosphere.2021.132187

Feng Y, Song K, Zhang W, Zhou X, Yoo SJ, Kim J-G, Qiao S, Qi Y, Zou X, Chen Z, Qin T, Yue N, Wang Z, Li D, Zheng W (2022) Efficient ORR catalysts for zinc-air battery: biomass-derived ultra-stable Co nanoparticles wrapped with graphitic layers via optimizing electron transfer. J Energy Chem 70:211–218. https://doi.org/10.1016/j.jechem.2022.01.047

Gabhi R, Basile L, Kirk DW, Giorcelli M, Tagliaferro A, Jia CQ (2020) Electrical conductivity of wood biochar monoliths and its dependence on pyrolysis temperature. Biochar 2(3):369–378. https://doi.org/10.1007/s42773-020-00056-0

He Z, Zhang J, Gong Z, Lei H, Zhou D, Zhang N, Mai W, Zhao S, Chen Y (2022) Activating lattice oxygen in NiFe-based (oxy)hydroxide for water electrolysis. Nat Commun 13(1):2191. https://doi.org/10.1038/s41467-022-29875-4

Hu C, Jin H, Liu B, Liang L, Wang Z, Chen D, He D, Mu S (2021) Propagating Fe-N₄ active sites with vitamin C to efficiently drive oxygen electrocatalysis. Nano Energy 82:105714. https://doi.org/10.1016/j.nanoen.2020.105714

Hui B, Chen HJ, Zhou CF, Cai LP, Zhang KW, Quan FY, Yang DJ (2022) Biochar aerogel-based electrocatalyst towards efficient oxygen evolution in acidic media. Biochar. https://doi.org/10.1007/s42773-022-00163-0

Jiang Z, Zou Y, Li Y, Kong F, Yang D (2021) Environmental life cycle assessment of supercapacitor electrode production using algae derived biochar aerogel. Biochar 3(4):701–714. https://doi.org/10.1007/s42773-021-00122-1

Lee S, Choi J, Kim M, Park J, Park M, Cho J (2022) Material design and surface chemistry for advanced rechargeable zinc-air batteries. Chem Sci 13(21):6159–6180. https://doi.org/10.1039/d1sc07212a

Li W, Liu B, Liu D, Guo P, Liu J, Wang R, Guo Y, Tu X, Pan H, Sun D, Fang F, Wu R (2022) Alloying Co species into ordered and interconnected macroporous carbon polyhedra for efficient oxygen reduction reaction in rechargeable zinc-air batteries. Adv Mater 34(17):e2109605. https://doi.org/10.1002/adma.202109605

Liang W, Chen J, Liu Y, Chen S (2014) Density-functional-theory calculation analysis of active sites for four-electron reduction of O₂ on Fe/N-doped graphene. ACS Catal 4(11):4170–4177. https://doi.org/10.1021/cs501170a

Liu D, Tong Y, Yan X, Liang J, Dou SX (2019) Recent advances in carbon-based bifunctional oxygen catalysts for zinc-air batteries. Batteries Supercaps 2(9):743–765. https://doi.org/10.1002/batt.201900052

Liu H, Liu Y, Mehdi S, Wu X, Liu T, Zhou B, Zhang P, Jiang J, Li B (2021) Surface phosphorus-induced CoO coupling to monolithic carbon for efficient air electrode of quasi-solid-state Zn-air batteries. Adv Sci 8(19):2101314. https://doi.org/10.1002/advs.202101314

Liu J, Li C, Ye Q, Lin L, Wang Y, Sun M, Cheng Y (2022a) Fe-doped Ni₂P porous nanofibers as highly efficient electrocatalyst for oxygen evolution reaction. Catal Commun 163:106416. https://doi.org/10.1016/j.catcom.2022.106416

Liu Q, Liu R, He C, Xia C, Guo W, Xu Z-L, Xia BY (2022b) Advanced polymer-based electrolytes in zinc–air batteries. eScience 2(5):453–466. https://doi.org/10.1016/j.esci.2022.08.004

Liu Z, Li H, Kang H-S, N'Diaye AT, Lee MH (2023) Lattice oxygen-mediated NiOOM formation for efficient oxygen evolution reaction in MOF@LDH core–shell structures. Chem Eng J 454:140403. https://doi.org/10.1016/j.cej.2022.140403

Lu X, Xue H, Gong H, Bai M, Tang D, Ma R, Sasaki T (2020) 2D layered double hydroxide nanosheets and their derivatives toward efficient oxygen evolution reaction. Nanomicro Lett 12(1):86. https://doi.org/10.1007/s40820-020-00421-5

Lu H, Tournet J, Dastafkan K, Liu Y, Ng YH, Karuturi SK, Zhao C, Yin Z (2021) Noble-metal-free multicomponent nanointegration for sustainable energy conversion. Chem Rev 121(17):10271–10366. https://doi.org/10.1021/acs.chemrev.0c01328

Lu F, Fan K, Cui L, Li B, Yang Y, Zong L, Wang L (2022) Engineering FeN$_4$ active sites onto nitrogen-rich carbon with tubular channels for enhanced oxygen reduction reaction performance. Appl Catal B 313:121464. https://doi.org/10.1016/j.apcatb.2022.121464

Lv Y, Wu X, Jia W, Guo J, Zhang H, Liu H, Jia D, Tong F (2020) Graphdiyne-anchored ultrafine NiFe hydroxide nanodots electrocatalyst for water oxidation with high mass activity and superior durability. Carbon 169:45–54. https://doi.org/10.1016/j.carbon.2020.07.048

Meftahi A, Shabani-Nooshabadi M, Reisi-Vanani A (2022) AgI/g-C$_3$N$_4$ nanocomposite as electrode material for supercapacitors: comparative study for its efficiency in three different aqueous electrolytes. Electrochim Acta 430:141052. https://doi.org/10.1016/j.electacta.2022.141052

Meftahi A, Reisi-Vanani A, Shabani-Nooshabadi M (2023a) Comparison of performance of CuI/g-C$_3$N$_4$ nanocomposites synthesized on Ni-foam and graphitic substrates as suitable electrode materials for supercapacitors. Fuel 331:125683. https://doi.org/10.1016/j.fuel.2022.125683

Meftahi A, Shabani-Nooshabadi M, Reisi-Vanani A (2023b) Introducing GO/CuI nanostructure as active electrode matter for supercapacitors: a comparative investigation within two aqueous electrolytes. J Energy Storage 63:107077. https://doi.org/10.1016/j.est.2023.107077

Mehmood A, Gong M, Jaouen F, Roy A, Zitolo A, Khan A, Sougrati M-T, Primbs M, Bonastre AM, Fongalland D, Drazic G, Strasser P, Kucernak A (2022) High loading of single atomic iron sites in Fe–NC oxygen reduction catalysts for proton exchange membrane fuel cells. Nat Catal 5(4):311–323. https://doi.org/10.1038/s41929-022-00772-9

Mohassel R, Soofivand F, Dawi EA, Shabani-Nooshabadi M, Salavati-Niasari M (2023) ErMnO$_3$/Er$_2$Mn$_2$O$_7$/ZnO/GO multi-component nanocomposite as a promising material for hydrogen storage: facile synthesis and comprehensive investigation of component roles. J Energy Storage 65:107285. https://doi.org/10.1016/j.est.2023.107285

Niu W-J, He J-Z, Gu B-N, Liu M-C, Chueh Y-L (2021) Opportunities and challenges in precise synthesis of transition metal single-atom supported by 2D materials as catalysts toward oxygen reduction reaction. Adv Funct Mater 31(35):2103558. https://doi.org/10.1002/adfm.202103558

Niu Y, Gong S, Liu X, Xu C, Xu M, Sun S-G, Chen Z (2022) Engineering iron-group bimetallic nanotubes as efficient bifunctional oxygen electrocatalysts for flexible Zn–air batteries. eScience 2(5):546–556. https://doi.org/10.1016/j.esci.2022.05.001

Pei Y, Ge Y, Chu H, Smith W, Dong P, Ajayan PM, Ye M, Shen J (2019) Controlled synthesis of 3D porous structured cobalt-iron based nanosheets by electrodeposition as asymmetric electrodes for ultra-efficient water splitting. Appl Catal B 244:583–593. https://doi.org/10.1016/j.apcatb.2018.11.091

Peng X, Zhang L, Chen Z, Zhong L, Zhao D, Chi X, Zhao X, Li L, Lu X, Leng K, Liu C, Liu W, Tang W, Loh KP (2019) Hierarchically porous carbon plates derived from wood as bifunctional ORR/OER electrodes. Adv Mater 31(16):e1900341. https://doi.org/10.1002/adma.201900341

Sadeghi M, Shabani-Nooshabadi M, Ansarinejad H (2023) A nanoporous gold film sensor modified with polypyrrole/CuO nanocomposite for electrochemical determination of piroxicam and tramadole. Environ Res 216(3):114633. https://doi.org/10.1016/j.envres.2022.114633

Sakhiya AK, Anand A, Kaushal P (2020) Production, activation, and applications of biochar in recent times. Biochar 2(3):253–285. https://doi.org/10.1007/s42773-020-00047-1

Shi Y, Li M, Yu Y, Zhang B (2020) Recent advances in nanostructured transition metal phosphides: synthesis and energy-related applications. Energy Environ Sci 13(12):4564–4582. https://doi.org/10.1039/d0ee02577a

Song H, Xu S, Li Y, Dai J, Gong A, Zhu M, Zhu C, Chen C, Chen Y, Yao Y, Liu B, Song J, Pastel G, Hu L (2018) Hierarchically porous, ultrathick, breathable wood-derived cathode for lithium-oxygen batteries. Adv Energy Mater 8(4):1701203. https://doi.org/10.1002/aenm.201701203

Tahernejad-Javazmi F, Shabani-Nooshabadi M, Karimi-Maleh H (2018) Analysis of glutathione in the presence of acetaminophen and tyrosine via an amplified electrode with MgO/SWCNTs as a sensor in the hemolyzed erythrocyte. Talanta 176:208–213. https://doi.org/10.1016/j.talanta.2017.08.027

Tang ZJ, Pei ZX, Wang ZF, Li HF, Zeng J, Ruan ZH, Huang Y, Zhu MS, Xue Q, Yu J, Zhi CY (2018) Highly anisotropic, multichannel wood carbon with optimized heteroatom doping for supercapacitor and oxygen reduction reaction. Carbon 130:532–543. https://doi.org/10.1016/j.carbon.2018.01.055

Tian YH, Xu L, Bao J, Qian JC, Su HN, Li HM, Gu HD, Yan C, Li HN (2019) Hollow cobalt oxide nanoparticles embedded in nitrogen-doped carbon nanosheets as an efficient bifunctional catalyst for Zn-air battery. J Energy Chem 33:59–66. https://doi.org/10.1016/j.jechem.2018.08.007

Wang Y, Kang J, Jiang S, Li H, Ren Z, Xu Q, Jiang Q, Liu W, Li R, Zhang Y (2020) A composite of Ni–Fe–Zn layered double hydroxides/biochar for atrazine removal from aqueous solution. Biochar 2(4):455–464. https://doi.org/10.1007/s42773-020-00066-y

Wang T, Cao X, Qin H, Shang L, Zheng S, Fang F, Jiao L (2021) P-Block atomically dispersed antimony catalyst for highly efficient oxygen reduction reaction. Angew Chem Int Ed Engl 60(39):21237–21241. https://doi.org/10.1002/anie.202108599

Wang Y, Chen Z, Zhang M, Liu Y, Luo H, Yan K (2022) Green fabrication of nickel-iron layered double hydroxides nanosheets efficient for the enhanced capacitive performance. Green Energy Environ 7(5):1053–1061. https://doi.org/10.1016/j.gee.2021.01.019

Wang C, Zhai P, Xia M, Liu W, Gao J, Sun L, Hou J (2023) Identification of the origin for reconstructed active sites on oxyhydroxide for oxygen evolution reaction. Adv Mater 35(6):2209307. https://doi.org/10.1002/adma.202209307

Wu XX, Chen KQ, Lin ZP, Zhang YM, Meng H (2019) Nitrogen doped graphitic carbon from biomass as non noble metal catalyst for oxygen reduction reaction. Mater Today Energy 13:100–108. https://doi.org/10.1016/j.mtener.2019.05.004

Wu K, Zhang L, Yuan Y, Zhong L, Chen Z, Chi X, Lu H, Chen Z, Zou R, Li T, Jiang C, Chen Y, Peng X, Lu J (2020) An iron-decorated carbon aerogel for rechargeable flow and flexible Zn-Air batteries. Adv Mater 32(32):2002292. https://doi.org/10.1002/adma.202002292

Xie H, Xie X, Hu G, Prabhakaran V, Saha S, Gonzalez-Lopez L, Phakatkar AH, Hong M, Wu M, Shahbazian-Yassar R, Ramani V, Al-Sheikhly MI, Jiang D-e, Shao Y, Hu L (2022) Ta–TiO$_x$ nanoparticles as radical scavengers to improve the durability of Fe–N–C oxygen reduction catalysts. Nat Energy 7(3):281–289. https://doi.org/10.1038/s41560-022-00988-w

Yan L, Xu Y, Chen P, Zhang S, Jiang H, Yang L, Wang Y, Zhang L, Shen J, Zhao X, Wang L (2020a) A freestanding 3D heterostructure film stitched by MOF-derived carbon nanotube microsphere superstructure and reduced graphene oxide sheets: a superior multifunctional electrode for overall water splitting and Zn-Air batteries. Adv Mater 32(48):2003313. https://doi.org/10.1002/adma.202003313

Yan W, Wu YL, Chen YL, Liu Q, Wang K, Cao N, Dai FN, Li XY, Jiang JZ (2020b) Facile preparation of N-doped corncob-derived carbon nanofiber efficiently encapsulating Fe$_2$O$_3$ nanocrystals towards high ORR electrocatalytic activity. J Energy Chem 44:121–130. https://doi.org/10.1016/j.jechem.2019.09.002

Yan B, Zheng J, Feng L, Du C, Jian S, Yang W, Wu YA, Jiang S, He S, Chen W (2022a) Wood-derived biochar as thick electrodes for high-rate performance supercapacitors. Biochar. https://doi.org/10.1007/s42773-022-00176-9

Yan L, Xu Z, Liu X, Mahmood S, Shen J, Ning J, Li S, Zhong Y, Hu Y (2022b) Integrating trifunctional Co@NC-CNTs@NiFe-LDH electrocatalysts with arrays of porous triangle carbon plates for high-power-density rechargeable Zn-air batteries and self-powered water splitting. Chem Eng J 446:137049. https://doi.org/10.1016/j.cej.2022.137049

Yang R, Zhou Y, Xing Y, Li D, Jiang D, Chen M, Shi W, Yuan S (2019) Synergistic coupling of CoFe-LDH arrays with NiFe-LDH nanosheet for highly efficient overall water splitting in alkaline media. Appl Catal B 253:131–139. https://doi.org/10.1016/j.apcatb.2019.04.054

Yang H, Dong C, Wang H, Qi R, Gong L, Lu Y, He C, Chen S, You B, Liu H, Yao J, Jiang X, Guo X, Xia BY (2022a) Constructing nickel-iron oxyhydroxides integrated with iron oxides by microorganism corrosion for oxygen evolution. Proc Natl Acad Sci USA 119(20):2202812119. https://doi.org/10.1073/pnas.2202812119

Yang H, Liu Y, Liu X, Wang X, Tian H, Waterhouse GIN, Kruger PE, Telfer SG, Ma S (2022b) Large-scale synthesis of N-doped carbon capsules supporting atomically dispersed iron for efficient oxygen reduction reaction electrocatalysis. eScience 2(2):227–234. https://doi.org/10.1016/j.esci.2022.02.005

Yang R, Guo X, Wu H, Kang W, Song K, Li Y, Huang X, Wang G (2022c) Anisotropic hemp-stem-derived biochar supported phase change materials with efficient solar-thermal energy conversion and storage. Biochar. https://doi.org/10.1007/s42773-022-00162-1

Ye S, Zeng G, Tan X, Wu H, Liang J, Song B, Tang N, Zhang P, Yang Y, Chen Q (2020) Nitrogen-doped biochar fiber with graphitization from *Boehmeria nivea* for promoted peroxymonosulfate activation and non-radical degradation pathways with enhancing electron transfer. Appl Catal B 269:118850

Ye Q, Wu J, Wu P, Rehman S, Ahmed Z, Zhu N (2021) Enhancing peroxymonosulfate activation by Co-Fe layered double hydroxide catalysts via compositing with biochar. Chem Eng J 417:129111. https://doi.org/10.1016/j.cej.2021.129111

Yuan K, Lutzenkirchen-Hecht D, Li L, Shuai L, Li Y, Cao R, Qiu M, Zhuang X, Leung MKH, Chen Y, Scherf U (2020) Boosting oxygen reduction of single iron active sites via geometric and electronic engineering: nitrogen and phosphorus dual coordination. J Am Chem Soc 142(5):2404–2412. https://doi.org/10.1021/jacs.9b11852

Zahedi F, Shabani-Nooshabadi M (2023) Porous structure Ni/CuCo$_2$O$_4$ core–shell as a novel type of three-dimensional electrode with facile fabrication and binder-free toward enhanced methanol oxidation and supercapacitor performances. Fuel 335:127083. https://doi.org/10.1016/j.fuel.2022.127083

Zhan T, Liu X, Lu S, Hou W (2017) Nitrogen doped NiFe layered hydroxide/reduced graphene oxide mesoporous nanosphere as an effective bifunctional electrocatalyst for oxygen reduction and evolution reactions. Appl Catal B 205:551–558. https://doi.org/10.1016/j.apcatb.2017.01.010

Zhang P, Liu Y, Wang S, Zhou L, Liu T, Sun K, Cao H, Jiang J, Wu X, Li B (2022) Wood-derived monolithic catalysts with the ability of activating water molecules for oxygen electrocatalysis. Small 18(34):e2202725. https://doi.org/10.1002/smll.202202725

Zhao J, Pu Z, Jin H, Zhang Z, Liu J, Mu S (2020) Phosphorous-doped carbon coordinated iridium diphosphide bifunctional catalyst with ultralow iridium amount for efficient all-pH-value hydrogen evolution and oxygen reduction reactions. J Catal 383:244–253. https://doi.org/10.1016/j.jcat.2020.01.026

Zhou W, Su H, Li Y, Liu M, Zhang H, Zhang X, Sun X, Xu Y, Liu Q, Wei S (2021) Identification of the evolving dynamics of coordination-unsaturated iron atomic active sites under reaction conditions. ACS Energy Lett 6(9):3359–3366. https://doi.org/10.1021/acsenergylett.1c01316

Zhou B, Liu Y, Wu X, Liu H, Liu T, Wang Y, Mehdi S, Jiang J, Li B (2022) Wood-derived integrated air electrode with Co-N sites for rechargeable zinc-air batteries. Nano Res 15(2):1415–1423. https://doi.org/10.1007/s12274-021-3678-3

Zhu J, Mu S (2020) Defect engineering in carbon-based electrocatalysts: insight into intrinsic carbon defects. Adv Funct Mater 30(25):2001097. https://doi.org/10.1002/adfm.202001097

Ziaie N, Shabani-Nooshabadi M (2023) Application of the C-C$_3$N$_4$/Li$_2$CoMn$_3$O$_8$//IL nanocomposite for design a sensitive electrochemical sensor inorder to detection of cetirizine, acetaminophen and phenylephrine in biological and pharmaceuticals samples. Environ Res 216(4):114667. https://doi.org/10.1016/j.envres.2022.114667